Solar Power Wires Based on Organic Photovoltaic Materials

Michael R. Lee, *et al.*

Science **324**, 232 (2009);
DOI: 10.1126/science.1168539

Science (print ISSN 0036-8075; online ISSN 1095-9203) is published weekly, except the last week in December, by the American Association for the Advancement of Science, 1200 New York Avenue NW, Washington, DC 20005.

shows the first branching-off event occurring at $z \approx -20$ cm. In both low- and high-energy cases, a complex nonlinear reshaping of the Airy wave packet takes place in which the high-intensity beam core develops a whiskerlike ghost beam that exhibits slightly faster acceleration compared to the primary Airy beam. The ghost beam is clearly visible in the high-intensity case. The beam reshaping features are well reproduced by the simulations that show both the whiskerlike structure and the faint satellite developing on propagation (Fig. 4, G to I).

The above observations suggest that the dominant lobe of the Airy beam acts as a "light bullet," an intense concentration of electromagnetic energy that travels along a curved trajectory and leaves a bent plasma channel behind. This wave packet is ~130 μm in diameter, 10 μm long (corresponding to the 35-fs-long pulse), and carries ~30% of the total energy of the laser pulse. Under these conditions, the wave packet's trajectory deviates from a straight line by over 2 mm, which is much larger than its size in both the transverse and longitudinal dimensions. For high pulse energies, secondary bullets bifurcate from the primary one but they quickly die out. The highly nonlinear propagation regime of the intense femtosecond Airy wave packet resembles that of a spatio-temporal soliton wave. What makes it markedly different is the fact that the Airy wave packet propagates along a curved trajectory, whereas known solitons in uniform media propagate along straight paths.

References and Notes

1. A. Braun *et al.*, *Opt. Lett.* **20**, 73 (1995).
2. Q. Luo *et al.*, *Appl. Phys. B* **82**, 105 (2006).
3. A. Proulx, A. Talebpour, S. Petit, S. L. Chin, *Opt. Commun.* **174**, 305 (2000).
4. C. D'Amico *et al.*, *Phys. Rev. Lett.* **98**, 235002 (2007).
5. C. P. Hauri *et al.*, *Appl. Phys. B* **79**, 673 (2004).
6. J. Kasparian *et al.*, *Opt. Express* **16**, 5757 (2008).
7. M. Mlejnek, E. M. Wright, J. V. Moloney, *Opt. Lett.* **23**, 382 (1998).
8. J. Kasparian *et al.*, *Science* **301**, 61 (2003).
9. A. Couairon, A. Mysyrowicz, *Phys. Rep.* **441**, 47 (2007).
10. D. Faccio *et al.*, *Phys. Rev. Lett.* **96**, 193901 (2006).
11. S. Tzortzakis *et al.*, *Opt. Lett.* **25**, 1270 (2000).
12. P. Polynkin *et al.*, *Opt. Express* **16**, 15733 (2008).
13. S. Akturk, B. Zhou, M. Franco, A. Couairon, A. Mysyrowicz, *Opt. Commun.* **282**, 129 (2009).
14. M. Châteauneuf, S. Payeur, J. Dubois, J.-C. Kieffer, *Appl. Phys. Lett.* **92**, 091104 (2008).
15. G. A. Siviloglou, J. Broky, A. Dogariu, D. N. Christodoulides, *Phys. Rev. Lett.* **99**, 213901 (2007).
16. G. A. Siviloglou, D. N. Christodoulides, *Opt. Lett.* **32**, 979 (2007).
17. G. A. Siviloglou, J. Broky, A. Dogariu, D. N. Christodoulides, *Opt. Lett.* **33**, 207 (2008).
18. M. V. Berry, N. L. Balazs, *Am. J. Phys.* **47**, 264 (1979).
19. I. M. Besieris, A. M. Shaarawi, *Opt. Lett.* **32**, 2447 (2007).
20. P. Saari, *Opt. Express* **16**, 10303 (2008).
21. M. Kolesik, J. V. Moloney, M. Mlejnek, *Phys. Rev. Lett.* **89**, 283902 (2002).
22. See supporting material on *Science* Online.
23. J. Broky, G. A. Siviloglou, A. Dogariu, D. N. Christodoulides, *Opt. Express* **16**, 12880 (2008).
24. J. Baumgartl, M. Mazilu, K. Dholakia, *Nat. Photonics* **2**, 675 (2008).

25. This work was supported by the U.S. Air Force Office of Scientific Research through grants FA9550-07-1-0010 and FA9550-07-1-0256. The contribution of G.A.S. and D.N.C. was partially supported by Lockheed Martin Corporation. We thank T.-M. O. Crust for stimulating discussions and D. Hansen and T. Milster for fabricating cubic phase masks used in the experiments.

Supporting Online Material

www.sciencemag.org/cgi/content/full/324/5924/229/DC1
Materials and Methods
SOM Text
References

9 December 2008; accepted 23 February 2009
10.1126/science.1169544

Solar Power Wires Based on Organic Photovoltaic Materials

Michael R. Lee, Robert D. Eckert, Karen Forberich, Gilles Dennler, Christoph J. Brabec, Russell A. Gaudiana*

Organic photovoltaics in a flexible wire format has potential advantages that are described in this paper. A wire format requires long-distance transport of current that can be achieved only with conventional metals, thus eliminating the use of transparent oxide semiconductors. A phase-separated, photovoltaic layer, comprising a conducting polymer and a fullerene derivative, is coated onto a thin metal wire. A second wire, coated with a silver film, serving as the counter electrode, is wrapped around the first wire. Both wires are encased in a transparent polymer cladding. Incident light is focused by the cladding onto to the photovoltaic layer even when it is completely shadowed by the counter electrode. Efficiency values of the wires range from 2.79% to 3.27%.

The use of organic and hybrid solar cells, based on nanostructured bulk heterojunction composites, represents a general approach toward flexible solar cells with reduced costs and size (*1*–*8*). The photoactive layer, as reported by Sariciftci *et al*. (*9*–*11*), consists of a conducting polymer and a solubilized fullerene derivative PCBM [(6,6)-phenyl-C_{61} butyric acid methyl ester]. These components, which are for the most part insoluble in one another, can be dissolved in a mutual solvent. When the resulting homogenous solution is coated as a thin layer on a substrate, the polymer and fullerene partially phase separate into intertwined wormlike or channel-like domains. This morphology creates an extremely high surface between the polymer phase (the electron donor) and the fullerene phase (the electron acceptor) that enhances the efficiency of electron collection.

If the cross-sectional dimension of the channels is in the range from 20 to 50 nm, excitons produced in the polymer phase, upon absorption of incident radiation, diffuse to the interface with the fullerene phase. At this interface, an electron from the excited state of the polymer is transferred to the fullerene phase. The hole, or cation, on the polymer chain, from which the electron was ejected, migrates to the secondary electrode by an electron/hole exchange mechanism between neighboring polymer chains. The electron in the fullerene phase hops from one fullerene molecule to another as it moves toward the primary electrode. The electrons flow from the primary electrode to an external load and reenter the cell via the secondary electrode. At the interface with the secondary electrode, each hole residing on the polymer chain picks up an electron, which converts it back to its ground state, thus completing the electrical circuit.

Theoretical studies have shown that the most recent generation of bulk heterojunction composites has an efficiency potential >10% for single junction devices (*12*) and 15% for dual junction (tandem) devices (*13*) that absorb in two different wavelengths, e.g., the visible and the near infrared.

One of the major difficulties with organic photovoltaics (OPV) wire technology is the thinness of the photoactive coatings, which can lead to shorting between the electrodes if their surface features exceed the combined layer thickness. Consequently, a wire core is required with a smooth surface in order to eliminate shorts resulting from large surface spikes. In addition, an n-type carrier counter electrode that is both highly conductive and optically transparent has not been reported. Even indium-tin oxide coatings with a resistivity as low as 10 ohm/cm^2 cannot transport the photocurrent generated with 1 sun irradiance over more than 10 to 15 mm without incurring electrical losses. Thus, we use one wire as the primary electrode for collecting electrons generated by the active layer, and we successively coat all three of the photocell layers, for example, the electron transport layer, the photoactive layer, and the hole transport layer, in sequence on top of one another, placing layer upon layer around the core wire. Each of the coatings

Konarka Technologies, Incorporated, Lowell, MA 01852, USA.

*To whom correspondence should be addressed. E-mail: rgaudiana@konarka.com

is deposited by drawing the core wire through a series of coating cups and drying ovens. The secondary electrode, for example, the counter electrode wire, is then wrapped under tension around the coated core wire. The idea that a second wire can be used to conduct electrons, provided that it contacts the surface of the primary wire along its entire length, is a key concept for making practical PV wires. Lastly, the wires are coated with a photocurable, transparent, protective polymer cladding.

Several attempts to make PV active wires or fibers have appeared in the recent literature. The organic-based fibers suffer from poor performance, for example, <1% efficiency, because of the use of thin, coated electrodes (*14*, *15*). Double wire-based dye-sensitized titania cells suffer from cracking with only 1% elongation and slight bending (*16*–*18*).

To begin the process of building an OPV wire, a stainless steel wire, which serves as the primary electrode, is coated with the photoactive layers. Stainless steel (ultrasmooth, 316 grade) exhibits a very useful combination of properties. It has high break strength, for example, 470 g, at small diameters (100 μm) and good conductivity (resistance = 94 ohm/m). The electrons generated by the photoactive layer at any location must travel no more than 100 nm before reaching the primary electrode. However, the holes on the polymers chains of the very thin active layer and hole transport layer on the core wire (circumference = 314 μm; the diameter of the primary electrode wire is 100 μm; see Fig. 1) must travel at most 157 μm to reach any point on the outer circumference where they come into contact with the secondary wire. Hence, a coating with a resistivity of 1 kohm/cm^2 is sufficient for efficient charge collection. The use of a highly conductive poly(3,4-ethylenedioxylenethiophene) (conductivity ~ 10 S/cm) hole transport layer can easily fulfill this requirement, and its transmission is >85% in the visible region of the spectrum. The coaxially wound counter electrode is also stainless steel (370 ohm/m, 50 μm). It is coated with a thin layer of silver paste, comprising both platelike and irregularly shaped silver particles, which improves the conductivity and acts as a smoothing layer. The coating is applied to the wire by drawing it through a coating cup and then drying at 120°C, where a uniform, 25-μm-thick conductive sheath of silver

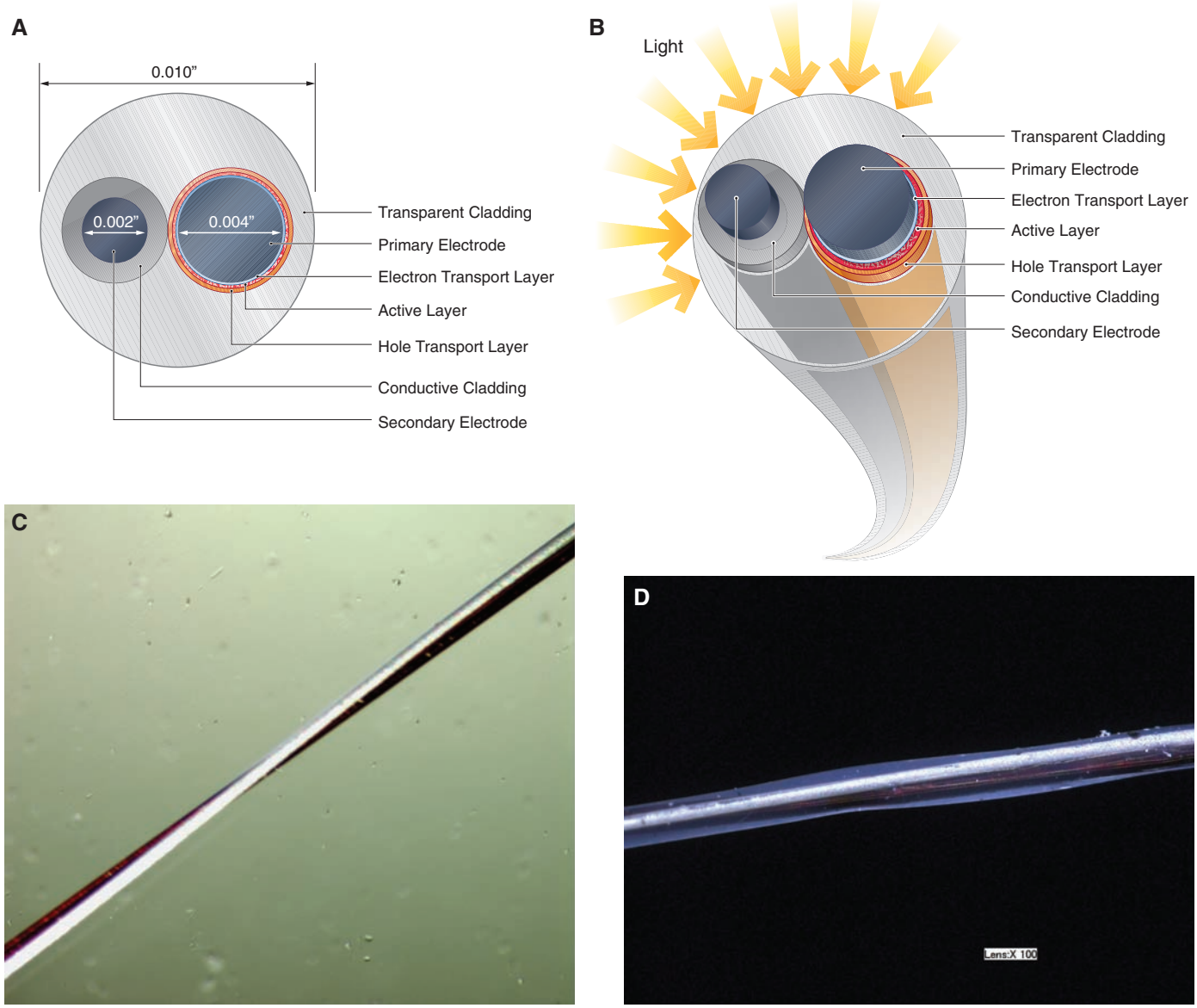

Fig. 1. (**A**) End-on schematic view of an OPV wire with the dimensions of the electrode wires and the coated layers; the photoactive layers on the primary electrode are not drawn to scale. (**B**) Schematic of a complete fiber showing the potential for shadowing by the secondary electrode. (**C**) Optical microscope picture of the silver-coated, secondary electrode wire (white) wrapped around the coated, primary electrode wire before cladding. (**D**) Digital microscope picture of a polymer-clad double wire.

forms around the wire. The resistance of a 1-m-long wire is 115 ohms, which makes it nearly as conductive as the primary wire. The wire is taken up on a spool before joining it to the primary wire.

The PV layers are coated successively on one another by means of a series of vertically aligned coating cups containing the coating solutions of each successive layer. The coating speeds range from 10 feet/min (3.048 m/min) to as high as 50 feet/min (15.24 m/min). Each coating cup has a hole in the bottom; the diameter of the hole is slightly larger than the diameter of the wire, which allows the wire to pass through without touching the walls of the orifice. In this process, the primary wire is drawn through a cup containing an isopropanol solution of tetra(*n*-butyl)titanate, after which it immediately enters an oven (90° to 100°C), which drives off the solvent. This process forms a smooth, thin, robust layer of TiO_x that serves as the electron transport layer.

Next the coated wire is drawn through a second coating cup containing a solution of the active layer, which in these examples is a 1:0.8 (weight/weight) mixture of poly(3-hexyl-2,5-thiophene) (P3HT, Merck KGaA, Darmstadt, Germany) and [(6,6)-phenyl-C_{61} butyric acid methyl ester] ($PC_{61}BM$, Solenne BV, Groningen, Netherlands). This coating is then dried in a second oven set at 120°C. The procedure is repeated for the hole transport layer, that is, the electron blocking layer, which is typically poly(3,4-ethylenedioxylenethiophene)–polystyrne sulfonate (PEDOT·PSS, Baytron P HC V4, H. C. Stark, Newton, Massachusetts) or one of its analogs (Fig. 1).

The physical and electrical contact between the two wires was accomplished by wrapping the secondary electrode wire around the coated primary wire in a precisely controlled manner by means of a rotating stage on which the spool of secondary wire is mounted. This process is similar to that used in commercial wire winding operations. One compete wrap is accomplished only every 1.25 cm. An optical microscope image (Fig. 1C) shows the white secondary electrode wire wrapped around the reddish-brown primary wire. Electrical contact is maintained because the wrapped pair was kept under tension while pulling them through a coating cup containing a solventless, liquid, photocurable epoxide. Immediately upon exiting the coating cup, the wires enter an ultraviolet irradiation chamber, which rapidly polymerizes and hardens the cladding (Fig. 1D). The process for generating photoactive, clad wires has been developed to the point where it is now capable of routinely producing several hundred feet of PV wire for any given experiment (fig. S2D).

The photovoltaic performance of the OPV wire was determined in a manner similar to that used for flat cells and modules. Lengths of wire, ranging from 5 to 30 cm cut from the large spool, were placed in a calibrated solar simulator with an irradiance of 100 mW/cm^2 at AM 1.5. Raw data from the solar simulator were corrected for the spectral mismatch of P3HT/PCBM via external quantum efficiency measurements, which resulted in ~5% deviation to the true AM 1.5 values. The instrument was also cross-calibrated by remeasuring organic solar cells that were earlier certified by the National Renewable Energy Laboratory and the National Institute of Advanced Industrial Science and Technology. The area of the wire was taken as its length multiplied by the

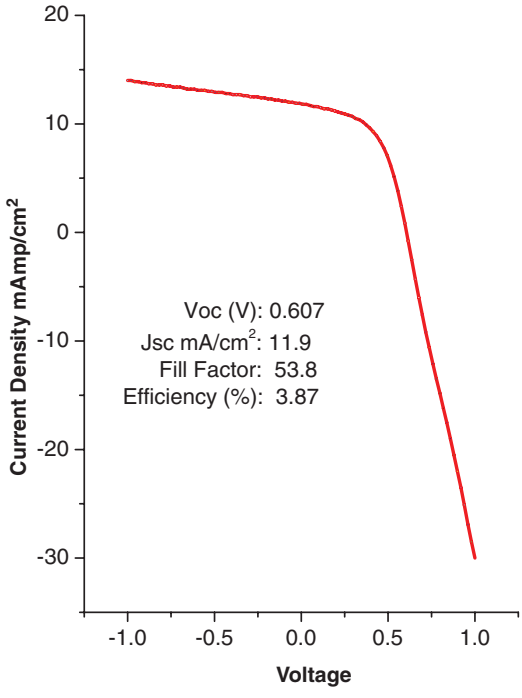

Fig. 2. *I-V* curve for a PV wire with the best performance observed thus far. J_{sc} indicates short circuit current.

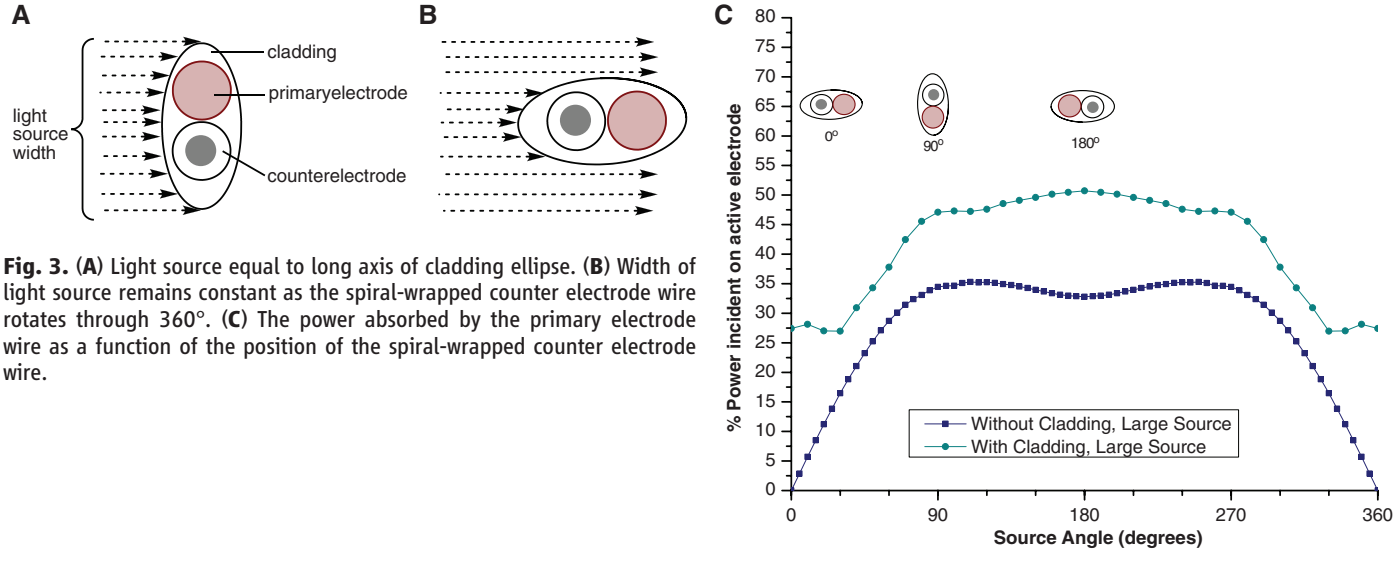

Fig. 3. (**A**) Light source equal to long axis of cladding ellipse. (**B**) Width of light source remains constant as the spiral-wrapped counter electrode wire rotates through 360°. (**C**) The power absorbed by the primary electrode wire as a function of the position of the spiral-wrapped counter electrode wire.

diameter of the primary electrode wire, for example, 100 μm, which is the projected area. No corrections are made for optical losses resulting from reflections from the curved air/cladding interface or the curvature of the primary wire or for shadowing from the spiral-wrapped secondary electrode wire, which is estimated to be 32% (Fig. 1C). This number was obtained by calculating the projection of the secondary electrode wire on the primary electrode wire at the currently used pitch. Shadowing of the primary wire may be altered by simply changing the pitch of the secondary electrode. Current-voltage (*I-V*) curves of 50 wire samples selected randomly from these long wires taken from many experimental spools exhibit an average efficiency of 2.99% (range from 2.79 to 3.27%). When the counter electrode is positioned completely behind the primary wire relative to the incident radiation, for example, no shadowing, the efficiency reaches 3.87%; an *I-V* curve of one of the latter is shown in Fig. 2.

Many of the wire cell parameters are equivalent typically to those exhibited by flat cells. In the best cell, the open circuit voltage (V_{oc}) is >0.6 mV, and the short circuit current density is 11.9 mA/cm^2. The current density in high-performance flat cells with the same materials in the active layer is usually in the range of 10 to 11 mA/cm^2; the highest reported is 11.5 mA/cm^2 (*19*). The origin of this unexpectedly high value exhibited by the wire is related to the optics of the double wire system. The efficiency of the wire is reduced because of the fill factor (FF = 53.8%), which in flat cells is typically around 60%. The lower value here is likely the result of incomplete contact between the wires.

The optical properties of the cladding along with the geometry of this coaxial wire system were examined in order to gain insight into the origin of the unexpectedly high current density. Ray tracing analysis was performed in order to evaluate the amount of light incident on the active layer coated wire when it is shadowed to various levels by the spiral-wrapped counter electrode wire (Fig. 3). The geometry of the model used for this analysis comprises two circular cylinders, representing the electrode wires, embedded in an elliptical cylinder of transparent cladding (refractive index = 1.49); this is an accurate representation of the shape of polymer cladding at any position along the wires. Light striking the primary electrode is assumed to be completely absorbed, whereas the silver-coated counter electrode acts as a diffuse reflector; the silver coating has a measured diffuse reflectivity ranging from 42 to 54% across the visible spectrum. Because the counter electrode wire is spirally wound around the primary electrode wire, shadowing of the latter ranges from complete shadowing to no shadowing. In this model, the width of the light source is held constant and set equal to the long axis of the ellipse. The estimated percent of the power absorbed by the primary electrode is a function of the position of the counter electrode.

When the counter electrode completely shadows the primary (e.g., 0°), the cladding focuses the incident light onto the primary wire, which allows it to capture 30% of the incident radiation (green line) compared with 0% without the cladding (blue line). At 180°, where the primary electrode faces the incident light source, the cladding focuses the light and improves incident power absorption by 18% compared with the unclad fiber, for example, 51% versus 33%, respectively. At angles between 0°, 180°, and 360° (especially between 100° to 140° and 220° to 260°), the power produced by the primary wire is partially from light reflected from the counter electrode. For the clad wires, this effect is evidenced by the shoulders in the same range of angles. The results clearly indicate that shadowing by the counter electrode is partially compensated by the lensing effect of the cladding and, to a lesser but nonnegligible extent, by diffuse reflection from the counter electrode.

Another approach to estimating the potential of this coaxial wire system is to determine the number of photons striking the active layer. We consider only two parameters: (i) the refractive index of the cladding and (ii) the distance of the point of incidence from the center of the fiber core. The photon count can be calculated by geometric optics; the transmission coefficients of the rays at the air-cladding interface were determined via the Fresnel formulas. We can estimate efficiency by plotting the light management factor in the photovoltaic wire as a function of the refractive index and the ratio of the primary wire diameter to the cladding diameter (Fig. 4). This factor is defined as the number of photons incident on the active layer of the wire with cladding, divided by the number of photons for a wire without cladding. When the ratio of the diameters is taken as 0.5, for example, the wire core is 100 μm, and the cladding is 200 μm; a cladding with a refractive index of 1.6 gives a light management factor of 1.42, which means that it can enhance the number of photons impinging the photoactive wire by more than 40% relative to a cladding with a refractive index of 1.4. A larger cladding with a higher refractive index could potentially capture energy that would otherwise be lost.

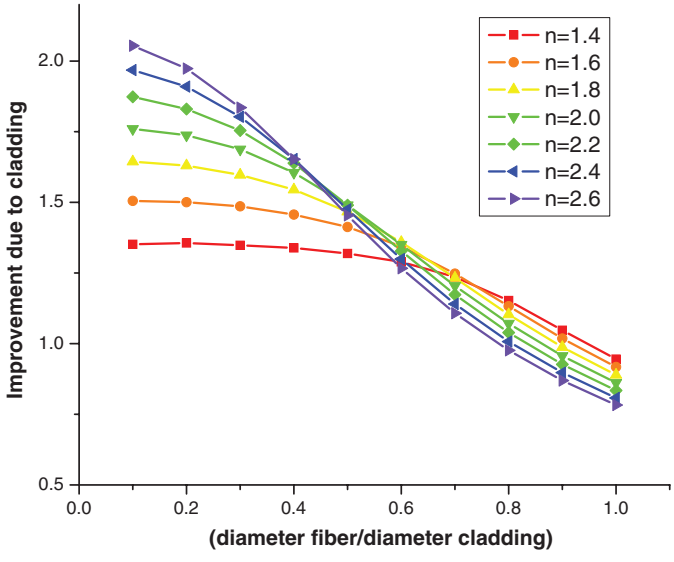

Fig. 4. Enhancement factor for the J_{sc} for different values of the refractive index of the OPV fiber and the ratio of the diameter of fiber and cladding.

References and Notes

1. G. Yu, J. Gao, J. C. Hummelen, F. Wudl, A. J. Heeger, *Science* **270**, 1789 (1995).
2. G. Yu, A. Gang, A. J. Heeger, *Synth. Met.* **85**, 1183 (1997).
3. L. Schmidt-Mende *et al.*, *Science* **293**, 1119 (2001).
4. Y. Kim *et al.*, *Nat. Mater. Lett.* **5**, 197 (2006).
5. J. Y. Kim *et al.*, *Science* **317**, 222 (2007).
6. J. Peet *et al.*, *Nat. Mater.* **6**, 497 (2007).
7. B. O'Regan, M. Graetzel, *Nature* **353**, 737 (1991).
8. W. U. Huynh, J. J. Dittmer, A. P. Alivisatos, *Science* **295**, 2425 (2002).
9. N. S. Sariciftci, L. Smilowitz, A. J. Heeger, F. Wudl, *Science* **258**, 1474 (1992).
10. N. S. Sariciftci, A. J. Heeger, U.S. Patent 5,454,880 (1994).
11. N. S. Sariciftci, A. J. Heeger, U.S. Patent 5,331,183 (1992).
12. M. C. Scharber *et al.*, *Adv. Mater.* **18**, 789 (2006).
13. G. Dennler *et al.*, *Adv. Mater.* **20**, 579 (2008).
14. J. Liu, M. A. G. Namboothiry, D. L. Carroll, *Appl. Phys. Lett.* **90**, 133515 (2007).
15. B. O'Connor, K. P. Pipe, M. Shtein, *Appl. Phys. Lett.* **92**, 193306 (2008).
16. J. Ramier *et al.*, *Thin Solid Films* **516**, 1913 (2008).
17. J. Ramier *et al.*, *Renewable Energy* **33**, 314 (2008).
18. X. Fan *et al.*, *Adv. Mater.* **20**, 592 (2008).
19. M. D. Irwin, D. B. Buchholz, A. W. Hains, R. P. H. Chang, T. J. Marks, *Proc. Natl. Acad. Sci. U.S.A.* **105**, 2783 (2008).

20. We would like to thank the ARMY Soldier Center (Natick, MA) for their support of this work. We acknowledge the following related patents, PCT/US2006/039364 and U.S. Patent 6,913,713.

Supporting Online Material

www.sciencemag.org/cgi/content/full/1168539/DC1
Materials and Methods
Figs. S1 and S2

14 November 2008; accepted 23 February 2009
Published online 12 March 2009;
10.1126/science.1168539
Include this information when citing this paper.